NANO LETTERS

Letter

pubs.acs.org/NanoLett

High-Responsivity Mid-Infrared Graphene Detectors with Antenna-Enhanced Photocarrier Generation and Collection

Yu Yao,[†] Raji Shankar,[†] Patrick Rauter,[†] Yi Song,[‡] Jing Kong,[‡] Marko Loncar,[†] and Federico Capasso*[,†]

[†]School of Engineering and Applied Sciences, Harvard University, Cambridge, Massachusetts 02138, United States

[‡]Department of Electrical Engineering and Computer Science, Massachusetts Institute of Technology, Cambridge, 02139, United States

Supporting Information

ABSTRACT: Graphene is an attractive photoconductive material for optical detection due to its broad absorption spectrum and ultrashort response time. However, it remains a great challenge to achieve high responsivity in graphene detectors because of graphene's weak optical absorption (only 2.3% in the monolayer graphene sheet) and short photocarrier lifetime (<1 ps). Here we show that metallic antenna structures can be designed to simultaneously improve both light absorption and photocarrier collection in graphene detectors. The coupled antennas concentrate free space light into the nanoscale deep-subwavelength antenna gaps, where the graphene light interaction is greatly enhanced as a result of the ultrahigh electric field intensity inside the gap. Meanwhile, the metallic antennas are designed to serve as electrodes that collect the generated photocarriers very efficiently. We also elucidate the mechanism of photoconductive gain in the graphene detectors and demonstrate mid-infrared (mid-IR) antenna-assisted graphene detectors at room temperature with more than 200 times enhancement of responsivity (~0.4 V/W at λ_0 = 4.45 μm) compared to devices without antennas (<2 mV/W).

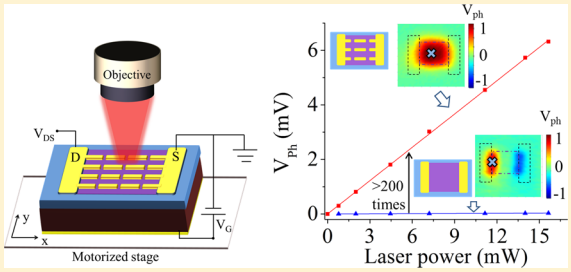

KEYWORDS: *Graphene, optical antennas, photodetectors, high speed, mid-infrared*

There has been significant interest in developing detectors in graphene due to its broad absorption from the ultraviolet (UV) to the far-infrared (FIR)[1] and ultrashort response time. Ultrafast graphene photodetectors in the near-infrared (near-IR) have been demonstrated with a bandwidth of over 40 GHz.[2,3] However, these detectors suffer from low responsivity (~5 mA/W), mainly due to the small optical absorption (~2.3%) and the short lifetime of photocarriers (~1 ps)[4−6] in graphene. Recent research has focused on enhancing optical absorption[7−12] and photocarrier multiplication[13−15] in graphene, while the low photocarrier collection efficiency, as a result of the short carrier lifetime, remains a limiting factor for high responsivity graphene detectors. One way to improve the responsivity is to increase the carrier lifetime by introducing carrier trapping mechanisms, which however also increases the detector response time to a few milliseconds or seconds.[16−18] The optimal strategy to achieve high responsivity without sacrificing the detector response time is to improve the photocarrier collection efficiency while maintaining the short carrier lifetime. Here we present an antenna-assisted graphene detector design, where optical antennas are used as both light-harvesting components and electrodes to simultaneously enhance light absorption and carrier collection efficiency. We have experimentally demonstrated mid-IR graphene detectors with more than 200 times enhancement of responsivity at room temperature, which are highly desirable for applications in mid-IR spectroscopy and imaging,[19,20] biochemical sensing,[21] environmental monitoring, and health diagnostics.[22]

Design of Antenna-Assisted Graphene Detectors. The antenna-assisted graphene detectors are composed of end-to-end coupled antennas on a graphene sheet, as shown in Figure 1a. The electrical field intensity enhancement distribution ($|E|^2/|E_0|^2$) at the antenna resonance wavelength λ_R = 4.45 μm is obtained by finite difference time domain (FDTD) simulations and also shown Figure 1a. Light incident from free space is tightly concentrated into the near-field in the nanogaps between antennas (gap size ~100 nm), which can greatly enhance the light−graphene interaction[23] and thus increase light absorption in graphene. A layer of palladium (Pd) film (thickness = 10 nm) beneath the gold antennas is used to minimize the contact resistance between the graphene and the antenna electrodes.[24] The electrical transport behavior of this antenna−graphene structure is simulated with finite element method (FEM) using the measured graphene sheet resistance and graphene−metal contact resistance of our sample (see Methods for more details). According to the simulation results, the resistance of the antenna-assisted graphene detector at a gate voltage $V_G = V_{CNP}$ = 5 V (V_{CNP} is the gate voltage when the concentrations of electrons and holes in the graphene sheet

Received: February 14, 2014
Revised: June 11, 2014
Published: June 18, 2014

   dx.doi.org/10.1021/nl500602n | *Nano Lett.* 2014, 14, 3749−3754

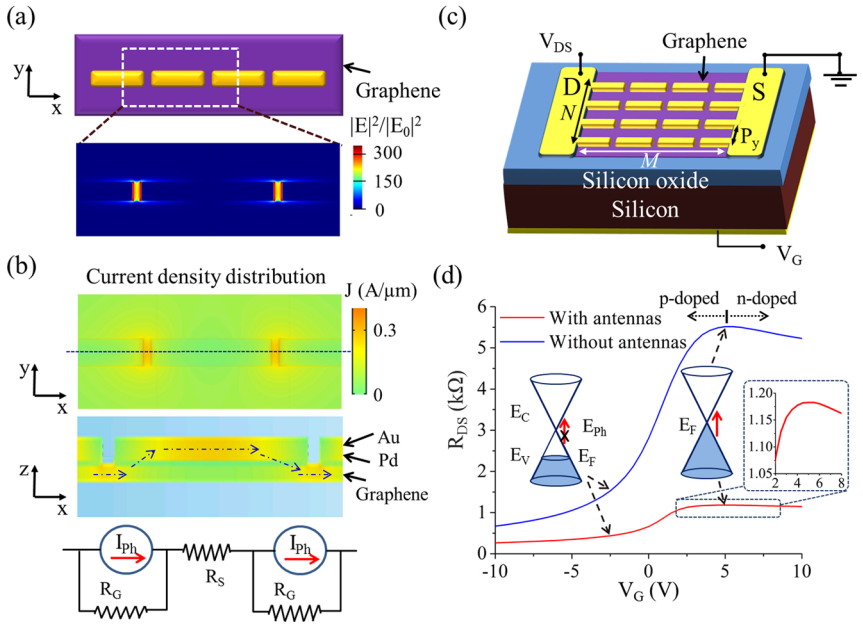

Figure 1. Design of the antenna-assisted graphene photodetector. (a) Top view of the end-to-end coupled antennas on graphene (top) and the electric field intensity enhancement distribution in the *xy*-plane, relative to the incident plane wave, calculated at 1 nm above the graphene surface (bottom). (b) Top: top view of the current density distribution in the graphene sheet. Middle: cross-sectional view of the current density distribution in the middle plane of the antenna (indicated by the dashed line in the top view), the dash-dotted arrows indicate the path of the current flow. Bottom: the equivalent circuit model of the antenna-assisted photoconductors. (c) A 3D schematic of the antenna-assisted graphene photodetector on a silicon substrate. The device has N rows and M columns of antennas. (d) The measured resistances between the two electrodes R_{DS} of the graphene detectors with and without antennas as a function of the gate voltage. Insets: band structures of graphene for two different gate voltages and a zoomed-in view of a portion of the curve close to the maximum resistance. The asymmetric resistance on the two sides of the Dirac point is due to the p-n-p junctions formed when the graphene channel is n-doped while the graphene underneath the Pd contact layer is p-doped as a result of the metal doping effect.[33] The area of the square graphene sheet is 900 μm^2. The metallic antenna structures in all the simulations and measurements in this figure are 0.95 μm long, 0.24 μm wide, and 40 nm thick (Pd thickness is 10 nm and Au thickness is 30 nm, greater than the skin depth (~10 nm) in Au at mid-IR wavelengths). The antenna gap size is 60 nm. The whole antenna array is composed of N = 24 rows (lateral period P_y = 1.2 μm), each comprising M = 30 end-to-end coupled antennas.

are equal) is about 24% of that of the reference device (the only difference between the reference devices and the antenna-assisted detectors is that the former do not have antennas on the graphene sheet). The simulated current density distribution in a portion of the graphene-antenna structure for a bias voltage V_{DS} = 0.6 V and a gate voltage V_G = 5 V is shown in Figure 1b. The current density distribution clearly shows that the current flows from one antenna to the graphene in the gap and then to the next antenna, as indicated by the dash-dotted arrows on the cross-section view. These results indicate that the current path through the metallic antennas has much lower resistance than that in the graphene sheet, thanks to the low contact resistance between the Pd layer and graphene. Thus, the antenna rods act like nanoelectrodes, which can effectively collect photocarriers generated in the nanogap between antennas because the carrier transit time across the gap can be shortened to subpicosecond time-scale for gap sizes ~100 nm (60 nm in our designs). In this nanodetector, the regions with high carrier collection efficiency automatically overlap with the regions where the light is concentrated and the majority of photocarriers are generated. Therefore, light absorption and photocarrier collection efficiency can be enhanced simultaneously. Note that a linear array of coupled antennas in Figure 1a is essentially a serial circuit of nanodetectors, the equivalent circuit of which is shown in the bottom of Figure 1b. Each nanodetector is composed of a pair of end-to-end coupled antennas and the graphene sheet beneath the antenna gap with a total area of ~0.4 μm^2. The ultracompact size of the nanodetector is highly desirable for reducing power dissipation, area, and increasing the bandwidth.[25]

Light detection in such nanodetectors is based on a photoconductor mechanism and the photocurrent responsivity is given by the following relation (see the derivation in the Supporting Information I)

$$R_A = \frac{R_G}{R_G + R_S + R_L}\frac{e}{h\nu}\alpha G \tag{1}$$

where R_G is the resistance of the graphene between the electrodes, R_S is the serial resistance due to the metal graphene contact, R_L is the load resistance, $h\nu$ is the photon energy, α is the fraction of the incident light absorbed in graphene, and G is the photoconductive gain

$$G = \frac{2M\tau_R}{\tau_{tr}}(1 - e^{-\tau_{tr}/\tau_R}) \tag{2}$$

which is defined as the ratio between the number of photocarriers collected by the electrodes and the number of photons absorbed in graphene. M is the hot carrier multiplication factor,[13−15] which scales linearly with photon energy and approaches unity in the mid-IR wavelength range.[15] τ_R is the carrier recombination time and τ_{tr} is the carrier transit time across the gap, given by $\tau_{tr} = g/v_d$, where g is the gap size and v_d is the carrier drift velocity. When the carrier transit time τ_{tr} is much shorter than its recombination lifetime τ_R, the photocarrier collection efficiency is close to 100% and the

dx.doi.org/10.1021/nl500602n | Nano Lett. 2014, 14, 3749−3754

photoconductive gain reaches its maximum value of 2. In other words, each photon absorbed in graphene results in two photocarriers, because the electrons and holes in single layer graphene have the same high mobility and thus both contribute to the photocurrent equally.

In our experiment, we designed graphene detectors with end-to-end coupled antenna structures in a 2D array (*M*-by-*N*, *M*, *N* are the numbers of columns and rows, respectively) to increase the light collection cross-section, as shown in Figure 1c. The device fabrication started with transferring a monolayer graphene sheet grown via chemical vapor deposition (CVD)) (see Supporting Information II for more details) onto a 30 nm-thick dry thermal oxide layer on a highly doped silicon substrate (P type, 0.001−0.005 Ω-cm). The antenna array was fabricated on the graphene sheet by electron beam lithography (EBL), electron beam evaporation of 10 nm Pd and 30 nm Au, and lift-off. Two contact pads (D and S, as indicated in the schematic in Figure 1c) are directly connected with the antennas on both sides of the array.

We first performed electrical transport characterization by measuring the resistance between the two contact pads S and D as a function of the gate voltage (see details in Methods), as shown in Figure 1d for a graphene detector with antennas and a reference detector of the same size but without antennas. The device with antennas has much lower resistance but almost the same charge neutral voltage V_{CNP}, which indicates that the intrinsic doping level of graphene in the antenna gap is not changed from its initial value by the presence of the metallic antennas. The decrease in resistance is because the current path through the metallic antennas has much lower resistance than that in the graphene sheet. At the gate voltage $V_G = V_{CNP} \approx 5$ V, the resistance for the antenna-graphene sample is ∼1.2 kΩ, ∼22% of that of the reference sample without antennas (∼5.5 kΩ), which shows very good agreement with the electrical transport simulations as discussed earlier. In the optical characterization of our detectors, we set the gate voltage close to $V_{CNP} \approx 5$ V to avoid Pauli blocking of the interband absorption of graphene[26] in the mid-IR range ($E_{Ph} \sim 100$ to 300 meV), as shown in Figure 1d.

Device Characterization. The optoelectronic characterization of the graphene detectors was performed in a setup as shown in Figure 2a. The sample was mounted on a 2D motorized stage. The output of a continuous wave (CW) quantum cascade (QC) laser (vacuum wavelength: $\lambda_0 = 4.45$ μm, close to the resonance of the antennas in the graphene detectors) was focused onto the sample by a mid-IR microscope objective (NA = 0.2). The diameter of the light spot size is estimated to be $2\lambda_0/\pi NA \approx 14$ μm. The local photovoltage response of the detectors was measured by scanning the position of the focused laser beam on the sample (see more details in Methods). The photovoltage maps of an antenna-assisted graphene detector (same design as the device in Figure 1d) and a reference detector with the same graphene sheet size and contact pads but without antennas are shown in Figure 2c,d, respectively (for both measurements, $V_G = 5$ V and $V_{DS} = 0.5$ V). In the reference detector, the photovoltages measured at the two electrodes in the reference detector have opposite signs due to the built-in potential at the graphene−metal (Pd) interface, as shown in Figure 2b. The photovoltage measured in the central region of the graphene sheet is almost negligible because of the short carrier lifetime and the long transit time to the electrodes. By contrast, the photovoltage map of the antenna-assisted graphene samples has the

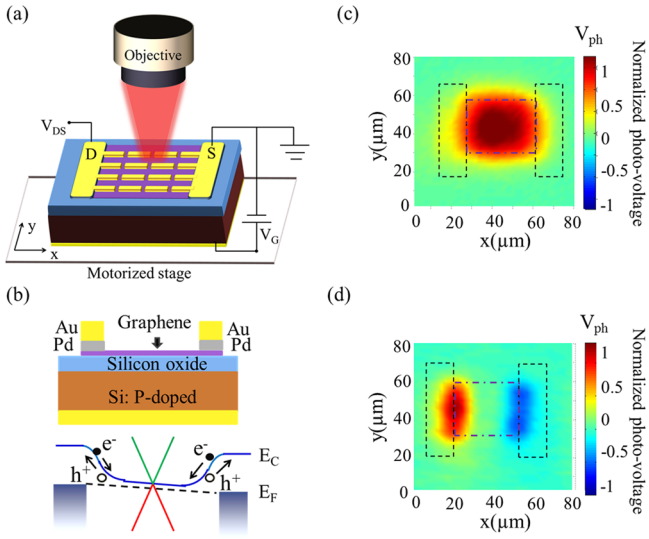

Figure 2. Photovoltage mapping of graphene photodetectors. (a) A 3D schematic of photocurrent measurement setup. (b) A cross-section view of the graphene detector without antennas (top) and its energy band diagram (bottom). The blue line indicates the potential profile of the conduction band edge (E_C). The green and red lines represent the conduction band and the valence band of graphene, respectively. The dashed black line shows the quasi Fermi level. The black dots and circles represent the photogenerated electrons (e^-) and holes (h^+), respectively. (c) The photovoltage map of the antenna-assisted graphene detector. (d) The photovoltage map of a graphene detector without antennas. The dashed lines and the dashed-dotted lines correspond to the position of the contact pads and the graphene sheet, respectively.

maximum value in the center and shows the same sign over the whole device region, because the number of photocarriers generated and collected by the antennas is much larger than that generated near the contact pads, which provides further evidence of highly improved responsivity by the antenna structures.

The wavelength dependent responsivity of the antenna-assisted graphene detector is measured with a wavelength tunable QC laser (wavelength range: 4.3 to 4.6 μm). As a result of the resonant nature of plasmonic antennas, the responsivity (photovoltage divided by the total incident power on the sample) exhibits strong wavelength dependence, as shown in Figure 3a for a device with the same structure design as that in Figure 1d. The responsivity reaches its maximum around 4.45 μm, which is very close to the peak wavelength (4.46 μm) of the electric field enhancement in the antenna gap calculated with FDTD simulation, also shown in the lower panel of Figure 3a.

The detector responsivity is also dependent on the bias of the detector, because the source drain bias influences the electric field within the graphene channel between adjacent antenna electrodes. As the bias current becomes larger, the responsivity increases monotonically and reaches its maximum ($R_V \approx 0.4$ V/W) at $I_{DS} \approx 4$ mA, as shown in Figure 3b. Further increasing the bias leads to reduced responsivity, probably because the electric field in the graphene channel (>2 MV/m) reaches its breakdown field. On the basis of the photovoltage responsivity of the detector array R_V, we calculated the photocurrent responsivity R_A of a single nanodetector $R_A = R_V N/R_G$ (see details in Methods) and extracted the photoconductive gain G using eq 1, as shown in Figure 3c. We used

dx.doi.org/10.1021/nl500602n | Nano Lett. 2014, 14, 3749−3754

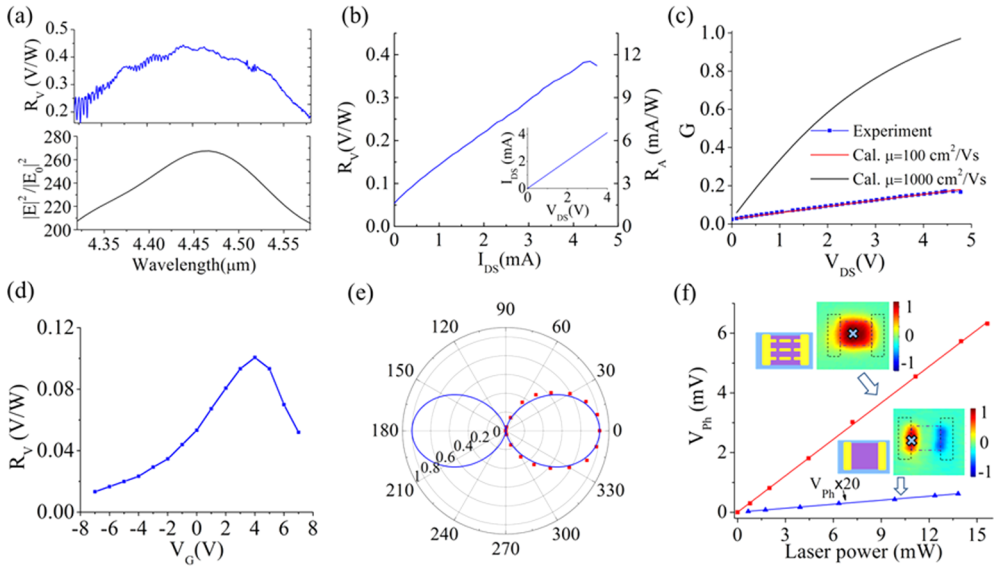

Figure 3. Device characterization of the antenna-assisted graphene detector. (a) Measured wavelength-dependent photoresponse of the antenna-assisted graphene detector (top) and electric field intensity enhancement in the center of the nanogap between the plasmonic antennas obtained with FDTD simulation (bottom). The antenna structures are the same as those in Figure 1. The narrow dips on the photoresponse curve are due to absorption lines of gas molecules in the air or on the sample (mainly CO_2). (b) Measured responsivity of the antenna-assisted graphene detector as a function of the biased current I_{DS} at V_{GS} = 4 V. The inset shows the V_{DS}–I_{DS} plot of the same detector when the laser is off. (c) The extracted photoconductive gain of the antenna-assisted graphene detector based on the measured detector responsivity and the calculated photoconductive gain for different graphene mobility (using the fitted value for photocarrier recombination time τ_R = 0.22 ps), as a function of V_{DS}. (d) Measured responsivity of the antenna-assisted graphene detector as a function of gate voltage. (e) Measured (solid red squares) and calculated (solid blue lines) normalized responsivity (with respect to the maximum value) of the antenna-assisted graphene detector for varying light polarization angle θ. (f) Measured photovoltage of the graphene detectors with and without antennas as a function of incident laser power. The crosses show the positions of the light spot on the sample during the measurement. All measurements are taken at room temperature.

τ_R as a parameter to fit the photoconductive gain with eq 2, where $\tau_{tr} = g/\mu E$ is determined by the gap size, the electric field in the graphene channel and the carrier mobility μ. The carrier mobility is estimated to be $\mu \approx 100$ cm^2/V$_S$ at V_G = 4 V for the graphene sample (see Methods for more detailed information). The photocarrier recombination time obtained from the fit is $\tau_R \approx 0.22$ ps. To achieve a high photoconductive gain, one needs to shorten the transit time τ_{tr}. Because τ_{tr} is proportional to the distance between the two electrodes g, the nanogap size (60 nm) in our detector design results in a much shorter τ_{tr} (about 2.8 ps at the maximum bias) than the devices without antennas ($\tau_{tr} \sim 100$ ps), which leads to a much higher photoconductive gain. An alternative way is to increase the graphene mobility. For CVD graphene, it is very practical to improve the mobility to 1000 cm^2/(V s), which gives a photoconductive gain over unity with our detector design, as also shown in Figure 3c. Figure 3d shows the detector responsivity as a function of gate voltage. It reaches the maximum at V_G = 4 V, where the Pauli blocking is still weak ($E_{Ph} > 2E_F$) and the photocarrier collection efficiency is larger due to the higher carrier mobility than that at the charge neutral point $V_G = V_{CNP}$ = 5 V.

The measured responsivity also shows a $\cos^2\theta$ dependence on the angle θ between the polarization of the incident light and the orientation of the antenna rods because only the component of the incident electric field parallel to the antenna rods (angle $\theta = 0°$) excites the antenna resonance. When the polarization is perpendicular to the antenna rod ($\theta = 90°$), the light intensity in the antenna gap will not be enhanced and the photocurrent generation in the graphene sheet is almost uniform. Figure 3e shows the measured detector responsivity as a function of angle θ, which agrees well with the calculation.

A comparison between the photoresponse of the graphene detectors with and without antennas is shown in Figure 3f. With antenna-enhanced photocarrier generation and collection, the photovoltage is increased by more than 200 times compared to that of the reference sample at the same laser power. According to the FDTD simulations, the absorption at the antenna resonance wavelength is enhanced by about 4–5 times (from ~2.3 to ~10%, see more details in Supporting Information III) compared with a pure monolayer graphene sheet. We attribute the additional 40–50 times improvement to the much more efficient carrier collection via metallic antennas. Moreover, the antenna-assisted graphene detector shows a linear photoresponse as the incident laser power increases up to 16 mW, indicating that the absorption is not saturated despite the strong field enhancement in the antenna gaps.

We also measured the time response of the detectors with a QC laser in pulsed mode operation, as shown in Figure 4. The output signal from the antenna-assisted detector was amplified with a preamplifier (40 dB, input impedance R_L= 500 ohms, bandwidth 400 MHz) and was then measured with an oscilloscope. On the basis of the exponential fits of the measurement (Figure 4, we estimated the time constants at the pulse rising and falling edges are very close, that is, 63 and 60 ns, respectively. Therefore, the detector response time is limited by the RC constant rather than the carrier lifetime. The detector RC constant is determined by the resistance (R_{DS}) and the parasitic capacitance (C_P) as well as the load capacitance (C_L) and resistance (R_L), that is, $\tau_{RC} = R_L R_{DS}(C_L + C_P/2)/(R_L + R_{DS}) \approx 30$ ns (see more details in Supporting Information IV). In comparison, the RC constant of the reference detector without antennas is estimated to be $\tau_{RC\_R} \approx 40$ ns, which is longer than that of the antenna-assisted detector because of a

dx.doi.org/10.1021/nl500602n | Nano Lett. 2014, 14, 3749–3754

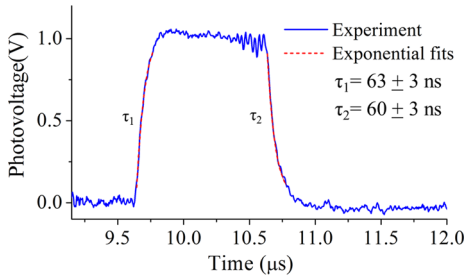

Figure 4. Response time of the antenna-assisted graphene detector. Measured output of the graphene detector when the light from a pulsed QC laser is incident on the detector (pulse width, 1 μs; repetition rate, 10 kHz).

higher source-drain resistance R_{DS}, as shown in Figure 1d. If we reduce the parasitic capacitance and minimize the load capacitance, the ultimate limit of the detector RC constant will be determined by the capacitance of the graphene-antenna structure $C_{DS,}$ that is, $\tau_{RC} \sim 0.01$ ps (see more details in Supporting Information IV). Another primary mechanism that limits the detector response time is the carrier transit time across the graphene channel between the two antenna electrodes, that is, $\tau_{tr} = g/v_d \approx 2.8$ ps $> \tau_{RC}$. Therefore, the transit time limited bandwidth is estimated to be $f_T = 3.5/2\pi\tau_{tr} \approx 600$ GHz,[2,27] which can be further increased by improving the graphene mobility.

Conclusion. We have demonstrated the use of metallic optical antennas to simultaneously enhance the optical absorption and photocarrier collection efficiency in graphene detectors and achieved room temperature mid-IR antenna-assisted graphene detectors with more than 200 times enhancement of responsivity compared to reference devices without antennas. Shrinking the detector element to deep subwavelength size is a promising solution to achieve high speed, ultracompact detectors with bandwidth up to terahertz range. This design concept can also be applied to the graphene detectors in other wavelength ranges, such as near IR and visible wavelength, and other thin film detectors. Moreover, the great flexibility in engineering antenna resonance properties enables a broad range of applications, such as spectrally selective photodetectors, multiwave imaging, and polarization-dependent measurement.

Methods. *Modeling and Simulation.* In the FDTD simulations (Lumerical Solutions Inc. http://www.lumerical.com/), the graphene layer is modeled as an anisotropic material with in-plane permittivity $\varepsilon_{\parallel}$ and out-of-plane permittivity $\varepsilon_{\perp}$. The former is calculated from the graphene sheet optical conductivity and the latter is assumed to be 2.5.[28] The antenna−graphene structures are placed on a 30 nm-thick SiO_2 layer on a silicon substrate.

We used finite element method (FEM, COMSOL Inc. http://www.comsol.com/) to simulate the electrical transport behavior of the antenna-assisted graphene detectors. The graphene layer is modeled as thin film of 20 nm with a sheet resistance the same as that obtained in the electrical transport measurements of the graphene sample (1.18 $k\Omega$/sq) at a gate voltage $V_G = V_{CNP} = 5$ V. The metal−graphene contact resistance is modeled with an ultrathin layer (2 nm) between metal and graphene. The resistivity of this layer is chosen so that the resistance between the metal and graphene is the same as the contact resistance (100 Ω/μm) measured at gate voltage $V_G = V_{CNP} = 5$ V. This configuration is justified by comparing the simulation results for the graphene sample and the measurement results, which gives a deviation less than 5%. A bias current (0.1 A) is applied between the two electrodes and the current distribution as well as the voltage drop between the electrodes is calculated with a stationary solver. The load resistance of each nanodetector in the detector array can be obtained based on the simulation results.

Relation between the Nanodetector Responsivity and the Detector Array Responsivity. Because the detector is composed by an array of nanodetectors (M-by-N, as shown in Figure 1c), the photovoltage contribution from one nanodetector is given by $V_{Ph} = R_V P_0/M$, where P_0 is the incident laser power on the array. For simplicity, we assume the laser power are uniformly distributed on all the nanodetectors, therefore, the power on each nanodetector is $P_0/(MN)$. On the basis of the circuit model for a single nanodetector (Figure 4b), the relation between V_{Ph} and the photocurrent responsivity of a nanodetector R_A is $V_{Ph} = R_G R_A P_0/NM$. Therefore, the photocurrent responsivity of a single nanodetector R_A is related to the detector array responsivity R_V by the expression $R_A = R_V N/R_G$.

Graphene Mobility Calculation. The mobility of the carrier is calculated from the measured gate dependent electric conductivity $\mu = e^{-1}\partial\sigma_G/\partial_n = e^{-1}\partial\sigma_G/\partial V_G \cdot \partial V_G/\partial_n$. The gate voltage dependence of the carrier concentration is given by $n \cong (n_0^2 + [C_d(V_G - V_{CNP})/e)^2]^{1/2}$, where n_0 is the residual carrier density at $V_G - V_{CNP}$.[29] It is estimated by $n_0 = \sigma_0 n_{imp} h/20e^2 \approx 8.1 \times 10^{11}$ for our graphene sample.[30]

Electrical and Optical Characterization. The conductance of graphene samples was measured using a parameter analyzer (Agilent 4156C) with varying gate voltages at room temperature. An integration time of 1 s was chosen for each data point. Note that the asymmetry of the graphene resistance in the n-type and p-type doped region originates from the p-doping of the graphene beneath the Pd electrodes and thus the formation of p-n or p-p junction in the graphene sheet between the electrodes,[31] rather than a difference in the electron and hole mobility. The contact resistance between metal and graphene was obtained by four-probe measurements.[32]

In the spatially resolved photovoltage measurement, we modulated the output from the CW QC laser with a chopper (frequency = 667 Hz) and measured the detector signal with a lock-in amplifier (model: SR810 DSP). The output of the lock-in amplifier was sent to the computer via a data acquisition board. The motorized 2D stage was computer-controlled and the photovoltage was recorded for each (x,y) position during the position scan of the device.

■ ASSOCIATED CONTENT

Supporting Information

The responsivity of graphene photoconductors, graphene growth and transfer, enhancement of absorption with antenna structures, and Detector RC constant calculation. This material is available free of charge via the Internet at http://pubs.acs.org.

■ AUTHOR INFORMATION

Corresponding Author

*E-mail: capasso@seas.harvard.edu (1-617-384-7611). Address: Pierce 205A, 29 Oxford Street, Cambridge, MA 02138.

Present Address

(P.R.) Institute of Semiconductor and Solid State Physics, Johannes Kepler University Linz, Linz, 4040, Austria.

Notes

The authors declare no competing financial interest.

■ ACKNOWLEDGMENTS

We gratefully acknowledge discussions with M. Kats, S. Byrnes, T. Mansuripur, and C. Wang. Device fabrication was performed at the Center for Nanoscale Systems, which is a member of the National Nanotechnology Infrastructure Network supported by the National Science Foundation (NSF). This research is supported in part by the Air Force Office of Scientific Research under Grant FA9550-12-1-0289 and by IARPA under Grant N66001-13-1-2007 vice N66001-13-1-3005. M. L. and R. S. gratefully acknowledge the financial support by NSF via the collaborative research Grant EECS-1028519.

■ REFERENCES

(1) Mak, K. F.; Ju, L.; Wang, F.; Heinz, T. F. *Solid State Commun.* **2012**, *152*, 1341−1349.
(2) Xia, F. N.; Mueller, T.; Lin, Y. M.; Valdes-Garcia, A.; Avouris, P. *Nat. Nanotechnol* **2009**, *4*, 839−843.
(3) Mueller, T.; Xia, F. N. A.; Avouris, P. *Nat. Photonics* **2010**, *4*, 297−301.
(4) Urich, A.; Unterrainer, K.; Mueller, T. *Nano Lett.* **2011**, *11*, 2804−2808.
(5) Winnerl, S.; Orlita, M.; Plochocka, P.; Kossacki, P.; Potemski, M.; Winzer, T.; Malic, E.; Knorr, A.; Sprinkle, M.; Berger, C.; de Heer, W. A.; Schneider, H.; Helm, M. *Phys. Rev. Lett.* **2011**, *107*, 237401.
(6) Dawlaty, J. M.; Shivaraman, S.; Chandrashekhar, M.; Rana, F.; Spencer, M. G. *Appl. Phys. Lett.* **2008**, *92*, 042116−042116-3.
(7) Fang, Z. Y.; Liu, Z.; Wang, Y. M.; Ajayan, P. M.; Nordlander, P.; Halas, N. J. *Nano Lett.* **2012**, *12*, 3808−3813.
(8) Furchi, M.; Urich, A.; Pospischil, A.; Lilley, G.; Unterrainer, K.; Detz, H.; Klang, P.; Andrews, A. M.; Schrenk, W.; Strasser, G.; Mueller, T. *Nano Lett.* **2012**, *12*, 2773−2777.
(9) Gan, X. T.; Shiue, R. J.; Gao, Y. D.; Meric, I.; Heinz, T. F.; Shepard, K.; Hone, J.; Assefa, S.; Englund, D. *Nat. Photonics* **2013**, *7*, 883−887.
(10) Pospischil, A.; Humer, M.; Furchi, M. M.; Bachmann, D.; Guider, R.; Fromherz, T.; Mueller, T. *Nat. Photonics* **2013**, *7*, 892−896.
(11) Wang, X. M.; Cheng, Z. Z.; Xu, K.; Tsang, H. K.; Xu, J. B. *Nat. Photonics* **2013**, *7*, 888−891.
(12) Freitag, M.; Low, T.; Zhu, W.; Yan, H.; Xia, F.; Avouris, P. *Nat. Commun.* **2013**, *4*, 1951.
(13) Winzer, T.; Knorr, A.; Malic, E. *Nano Lett.* **2010**, *10*, 4839−4843.
(14) Brida, D.; Tomadin, A.; Manzoni, C.; Kim, Y. J.; Lombardo, A.; Milana, S.; Nair, R. R.; Novoselov, K. S.; Ferrari, A. C.; Cerullo, G.; Polini, M. *Nat. Commun.* **2013**, *4*, 1987.
(15) Tielrooij, K. J.; Song, J. C. W.; Jensen, S. A.; Centeno, A.; Pesquera, A.; Elorza, A. Z.; Bonn, M.; Levitov, L. S.; Koppens, F. H. L. *Nat. Phys.* **2013**, *9*, 248−252.
(16) Konstantatos, G.; Badioli, M.; Gaudreau, L.; Osmond, J.; Bernechea, M.; de Arquer, F. P. G.; Gatti, F.; Koppens, F. H. L. *Nat. Nanotechnol* **2012**, *7*, 363−368.
(17) Zhang, B. Y.; Liu, T.; Meng, B.; Li, X.; Liang, G.; Hu, X.; Wang, Q. J. *Nat. Commun.* **2013**, *4*, 1811.
(18) Liu, C.-H.; Chang, Y.-C.; Norris, T. B.; Zhong, Z. *Nat. Nano* **2014**, *9*, 273−278.
(19) Tittel, F. K.; Richter, D.; Fried, A. *Top Appl. Phys.* **2003**, *89*, 445−510.
(20) Guo, B. J.; Wang, Y.; Peng, C.; Zhang, H. L.; Luo, G. P.; Le, H. Q.; Gmachl, C.; Sivco, D. L.; Peabody, M. L.; Cho, A. Y. *Opt Express* **2004**, *12*, 208−219.
(21) Young, C.; Kim, S. S.; Luzinova, Y.; Weida, M.; Arnone, D.; Takeuchi, E.; Day, T.; Mizaikoff, B. *Sens. Actuators, B* **2009**, *140*, 24−28.
(22) Seddon, A. B. *Phys. Status Solidi B* **2013**, *250*, 1020−1027.
(23) Yao, Y.; Kats, M. A.; Genevet, P.; Yu, N. F.; Song, Y.; Kong, J.; Capasso, F. *Nano Lett.* **2013**, *13*, 1257−1264.
(24) Huang, B. C.; Zhang, M.; Wang, Y. J.; Woo, J. *Appl. Phys. Lett.* **2011**, *99*, 032107.
(25) Krishnamoorthy, A. V.; Miller, D. A. B. *IEEE J. Sel. Top. Quantum Electron.* **1996**, *2*, 55−76.
(26) Wang, F.; Zhang, Y.; Tian, C.; Girit, C.; Zettl, A.; Crommie, M.; Shen, Y. R. *Science* **2008**, *320*, 206−9.
(27) Kato, K.; Hata, S.; Kawano, K.; Kozen, A. *IEICE Trans. Electron.* **1993**, *E76*, 214−221.
(28) Falkovsky, L. A. *J. Phys.: Conf. Ser.* **2008**, *129*, 012004.
(29) Meric, I.; Han, M. Y.; Young, A. F.; Ozyilmaz, B.; Kim, P.; Shepard, K. L. *Nat. Nanotechnol* **2008**, *3*, 654−659.
(30) Adam, S.; Hwang, E. H.; Galitski, V. M.; Das Sarma, S. *Proc. Natl. Acad. Sci. U.S.A.* **2007**, *104*, 18392−18397.
(31) Huard, B.; Stander, N.; Sulpizio, J. A.; Goldhaber-Gordon, D. *Phys. Rev. B* **2008**, *78*, 121401(R).
(32) Xia, F. N.; Perebeinos, V.; Lin, Y. M.; Wu, Y. Q.; Avouris, P. *Nat. Nanotechnol* **2011**, *6*, 179−184.
(33) Liu, W. J.; Yu, H. Y.; Xu, S. H.; Zhang, Q.; Zou, X.; Wang, J. L.; Pey, K. L.; Wei, J.; Zhu, H. L.; Li, M. F. *IEEE Electron Device Lett.* **2011**, *32*, 128−130.